ACS Energy LETTERS

http://pubs.acs.org/journal/aelccp

Resolving the Hydrophobicity of the Me-4PACz Hole Transport Layer for Inverted Perovskite Solar Cells with Efficiency >20%

Kashimul Hossain,[†] Ashish Kulkarni,*[,†] Urvashi Bothra, Benjamin Klingebiel, Thomas Kirchartz, Michael Saliba, and Dinesh Kabra*

Cite This: *ACS Energy Lett.* 2023, 8, 3860−3867

Read Online

ACCESS | Metrics & More | Article Recommendations | Supporting Information

ABSTRACT: A [4-(3,6-dimethyl-9*H*-carbazol-9-yl)butyl]phosphonic acid (Me-4PACz) self-assembled monolayer (SAM) has been employed in perovskite devices demonstrating high efficiencies. However, a uniform perovskite layer does not form due to the hydrophobicity of Me-4PACz. Here, we tackle this challenge by adding a conjugated polyelectrolyte, poly(9,9-bis(3′-(*N*,*N*-dimethyl)-*N*-ethylammonium-propyl-2,7-fluorene)-*alt*-2,7-(9,9-dioctylfluorene)) dibromide (PFN-Br), to the Me-4PACz in a specific ratio, defined as Pz:PFN. With this mixing engineering strategy using Pz:PFN, the PFN-Br interaction with the A-site cation is confirmed via solution-state nuclear magnetic resonance studies. The narrow full widths at half-maxima of diffraction peaks and photoluminescence spectra of perovskite films reveal improved crystallization at the optimal mixing ratio of Pz:PFN. Interestingly, the mixing of PFN-Br additionally tunes the work function of the Me-4PACz and the built-in voltage in the solar cells. Devices employing the optimized Pz:PFN mixing ratio deliver an open-circuit voltage of 1.16 V and efficiency >20% for perovskites with a bandgap of 1.6 eV with high reproducibility and concomitant stability.

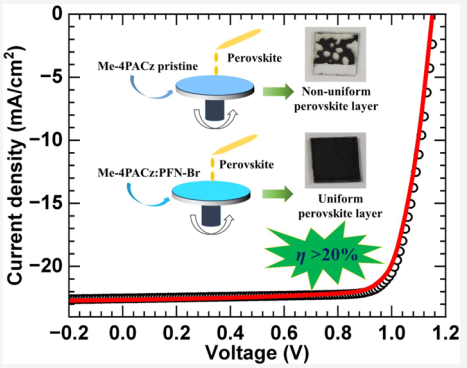

The power conversion efficiency (PCE) of perovskite solar cells (PSCs) has rapidly increased from 3.8% to a certified value of >25%.[1−3] This rapid rise in the PCE can be credited to excellent optoelectronic properties such as a high absorption coefficient, a low exciton binding energy, and a tunable bandgap.[4−8] The so-called inverted or *p-i-n* device architecture is of significant interest using low-temperature-processed charge transport layers (CTLs) such as poly(3,4-ethylenedioxythiophene) polystyrenesulfonate (PEDOT:PSS), poly(triaryl amine) (PTAA), and fullerene (C_{60}).[9−13] Recently, Al-Ashouri et al. used various phosphonic acid group-anchored carbazole-based self-assembled monolayers (SAMs) such as 2PACz, MeO-2PACz, and Me-4PACz as hole transport layers (HTLs), demonstrating superior device performance compared to the widely employed PTAA as HTL.[14−16] In particular, by employing a [4-(3,6-dimethyl-9*H*-carbazol-9-yl)butyl]phosphonic acid (Me-4PACz) SAM as the HTL, the same group reported one of the highest efficiency values in single-junction devices and a certified PCE of ∼29% in silicon−perovskite two-terminal tandem solar cells.[16] In comparison to other SAMs, the Me-4PACz-based device is reported to demonstrate the lowest density of interface traps, indicating suppressed nonradiative recombination at the perovskite/Me-4PACz interface.[17] These salient features make the Me-4PACz SAM a promising HTL for PSCs. Motivated by this, we fabricate PSCs with Me-4PACz as HTL. Unfortunately, we observed poor perovskite layer formation on the Me-4PACz, which is in line with other recent reports.[18−21] Strategies such as the incorporation of an Al_2O_3 insulating layer at the interface between Me-4PACz and perovskites and the deposition of Me-4PACz by evaporation have been reported to improve the perovskite layer coverage on Me-4PACz.[18,19,22] These strategies are promising, but developing a strategy to deposit Me-4PACz by a solution process and simultaneously obtain a uniform perovskite layer with improved device performance with a proper understanding remains a challenge.

Received: July 10, 2023
Accepted: August 14, 2023
Published: August 25, 2023

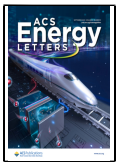

Until recently, the interface engineering approach has been applied to address the issue of poor wetting of perovskites on underlying hydrophobic polymeric HTLs. For instance, PTAA is known to be a hydrophobic HTL, and modification of its surface with poly(9,9-bis(3′-(*N*,*N*-dimethyl)-*N*-ethyl-ammoniumpropyl-2,7-fluorene)-*alt*-2,7-(9,9-dioctylfluorene))-dibromide (PFN-Br), poly(methyl methacrylate) (PMMA): 2,3,5,6-tetrafluoro-7,7,8,8-tetracyanoquinodimethane (F4-TCNQ), poly(vinyl oxide) (PEO), tetra-*n*-propylammonium bromide (TPAB), phenylethylammonium iodide (PEAI), etc. has been reported.[12,23−27] Among others, modification with PFN-Br has been widely employed, as it helps in obtaining a uniform perovskite layer with augmented device efficiency. Previously, we have also employed PFN-Br-modified PTAA and reported a PCE of >20%.[9] In addition to polymeric HTLs, modification of SAMs has also been reported.[28,29] Recently, Li et al. employed a mixture of MeO-2PACz and 2PACz to improve the charge extraction and reported a PCE of 25% for all-perovskite tandem solar cells.[29] Deng et al. showed that co-assembled monolayers (a mixture of SAM and alkyl-ammonium-containing SAM) can help in simultaneously suppressing the nonradiative recombination and surface functionalization, and the resultant device showed a PCE of 23.59%.[28] Very recently, Al-Ashouri added 1,6-hexylene-diphosphonic acid with Me-4PACz to improve the perovskite layer deposition; however, a detailed investigation has not been performed.[21] Until the present, the modification of carbazole-based SAMs has been limited to co-assembly with a phosphonic or carboxylic acid anchoring group, which might limit the exploration of the SAMs. Therefore, strategies need to be developed, beyond co-assembly with SAMs, to improve the perovskite layer coverage on Me-4PACz SAMs.

In this work, we report a mixing engineering strategy that combines Me-4PACz SAM with conjugated polyelectrolyte PFN-Br to obtain a highly reproducible and improved performance of PSCs. With the aid of mixed Me-4PACz:PFN-Br, a uniform perovskite thin film is obtained, and the device with an optimized Me-4PACz:PFN-Br mixing ratio showed a PCE of >20% for a 0.175 cm^2 device active area and 19% over an active area of 0.805 cm^2. To the best of our knowledge, the obtained device efficiency is one of the highest values reported for Me-4PACz with a triple-cation perovskite composition having a bandgap (E_g) of 1.6 eV. More importantly, with the help of solution nuclear magnetic resonance (NMR), X-ray diffraction (XRD), and Kelvin probe force microscopy (KPFM) outcomes, we elucidate the triple role of PFN-Br. PFN-Br interacts with the A-site cation and improves the crystallization. This also elevates the valence band position of Me-4PACz, leading to better interfacial energy level alignment with perovskite having a bandgap of 1.6 eV. We note that this improved performance could be achieved due to reduced interfacial localized states (low series resistance (R_S)) and bulk defects in the absorber layer (ideality factor $n \approx 1$), which not only result in high fill factor (*FF*), short-circuit current density (J_{SC}), and open-circuit voltage (V_{OC}) but also provide an excellent yield and stability for optimal PSCs. The unencapsulated device showed enhanced stability by retaining the initial device performance at T_{95} even after 3000 h when measured in ∼40% humidity conditions. Further, the operational stability at the 1-Sun condition and thermal stability at 85 °C of the unencapsulated device under a N_2 environment retain >90% of the initial efficiency after 300 and 600 h, respectively.

Me-4PACz has been used as HTL in single-junction and tandem (with silicon) devices, demonstrating one of the highest efficiencies.[16,17,30] In an attempt to fabricate the device using the Me-4PACz SAM, we observed poor perovskite layer formation. A schematic illustration of perovskite deposition on the Me-4PACz-coated ITO substrate and a photographic image (see also Video V1) of a perovskite thin film are shown in Figure 1a. The poor perovskite layer coverage can be

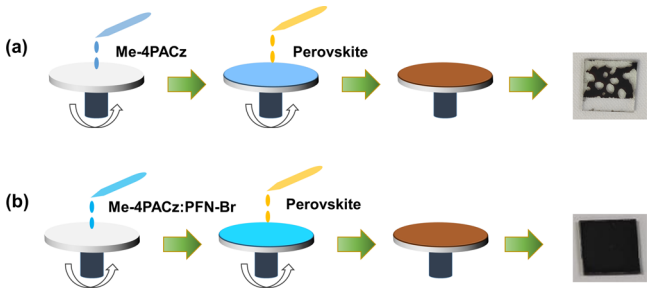

Figure 1. Schematic of the thin-film deposition of the Me-4PACz, Me-4PACz:PFN-Br (abbreviated as Pz:PFN), and perovskite layers. (a) Me-4PACz and perovskite layer deposition. (b) Deposition of mixed Me-4PACz:PFN-Br and perovskite layers.

attributed to the presence of nonpolar groups such as methyl ($-CH_3$) and long-alkyl chains (C_4H_8) in the Me-4PACz SAM, which are in general responsible for the hydrophobic nature.[31−35] To understand this more clearly, we performed water contact angle measurements of Me-4PACz to compare it with widely used hydrophobic polymer and small organic molecule-based HTLs such as PTAA, poly[2,6-(4,4-bis(2-ethylhexyl)-4*H*-cyclopenta[2,1-*b*;3,4-*b*′]dithiophene)-*alt*-4,7-(2,1,3-benzothiadiazole)] (PCPDTBT), poly(3-hexyl-thiophene-2,5-diyl) (P3HT), and 4,4′,4″-tris[phenyl(*m*-tolyl)-amino]triphenylamine (MTDATA). Figure S1 shows the molecular structure of the aforementioned HTLs and their respective water contact angles in comparison with Me-4PACz. As expected, the water contact angle for Me-4PACz is high and in the same range as those of other HTLs, evidencing its hydrophobic nature. We additionally washed the Me-4PACz-coated substrate with methanol (solvent to dissolve SAM; see the experimental details in the Supporting Information (SI)) in an attempt to reduce the hydrophobicity and obtain a uniform perovskite film. However, the perovskite layer showed non-uniform coverage, as can be seen in Figure S2. This indicates that the phosphonic acid group binds strongly with ITO and a strong monolayer fingerprint is present even after the washing step, in line with previous reports.[14] To further confirm the role of nonpolar groups that are present in Me-4PACz in preventing the perovskite layer formation, we fabricated a device by employing a 2PACz SAM as the HTL. Because of the absence of the $-CH_3$ group and long alkyl chain, not only was a uniform perovskite layer obtained but also the resultant device showed a PCE of ∼20%. This further confirms that, besides the SAM, all other layers of the device stack are working as expected. The current density (*J*)−voltage (*V*) curve of the best-performing device employing a 2PACz SAM is shown in Figure S3, and the device parameters are tabulated in Table S1. These results suggest that Me-4PACz is sufficiently hydrophobic to prevent the formation of a uniform perovskite layer, and strategies need to be developed to improve the perovskite layer coverage on the Me-4PACz SAM.

https://doi.org/10.1021/acsenergylett.3c01385
ACS Energy Lett. 2023, 8, 3860−3867

Typically, researchers have incorporated PFN-Br as an interlayer to modify the interface of hydrophobic polymeric HTLs and obtained a uniform perovskite layer.[23,36] We initially modified the surface of Me-4PACz with PFN-Br and obtained a uniform perovskite layer. The relevant discussion is mentioned in section ESI-1 in the SI, and the results are shown in Figures S4 and S5 and Table S2. The performance measures of these devices were low; therefore, we attempted a mixing engineering strategy. The steps involving deposition of device stack layers are schematically shown in Figure 1b. The Me-4PACz and PFN-Br were mixed in 6:4, 7:3, 8:2, 9:1, and 9.5:0.5 ratios, followed by the perovskite layer deposition by a one-step method (please see the experimental section in the SI for more details). From now onward, for our convenience, we term Me-4PACz:PFN-Br as Pz:PFN. Irrespective of all the mixing ratios, a uniform perovskite layer was obtained as shown in Figures 1b and S6. Top surface scanning electron microscope (SEM) images, Figure S7, showed no significant differences in the perovskite layer morphology with respect to the different Pz:PFN ratios. Moreover, we observed indistinct perovskite layer morphology on both the Me-4PACz/PFN-Br (termed Pz/PFN) (Figure S7a) dual layer and Me-4PACz (Figure S7g) compared to the mixing ratio cases. This further indicates that the perovskite layer crystallization is not influenced by the PFN-Br mixing or interlayer modification. The XRD diffractograms, as can be seen in Figure S8, showed no traces of residual lead iodide and no significant differences in the perovskite crystal structures. The combined outcomes of SEM and XRD indicate that perovskite crystallizes similarly in all cases without any significant changes. After the perovskite layer deposition, phenyl-C_{61}-butyric acid methyl ester (PCBM) and bathocuproine (BCP) were deposited via the solution process as an electron transport layer (ETL) and buffer layer, respectively, and the silver electrode was thermally evaporated to complete the cell. Figure 2a depicts the best-performing device $J-V$ curves in forward bias under 1-Sun illumination for all of the mixed Pz:PFN-based PSCs. The $J-V$ curves in forward and reverse scan directions are shown in Figure S9b, and the device parameters are tabulated in Table S3. With a change in the mixing ratio, the device performance first increased and then decreased. We note that there is a change in J_{SC} (also integrated J_{SC} from incident photon-to-current efficiency (IPCE)) with respect to the compositional ratio of the HTL, which will be discussed later along with KPFM results. The device obtained from Pz:PFN with a 9:1 ratio showed the highest PCE of 20.67%, with a J_{SC} of 22.54 mA/cm^2, V_{OC} of 1.16 V, and FF of 79.12%, with slight hysteresis (please see Table S3). Note that the obtained efficiency is one of the highest values reported with a Me-4PACz-based HTL and with a 1.6 eV bandgap PSC device, as shown in Figure S11, and the device parameters are tabulated in Table S4. The photovoltaic device performance over the 0.805 cm^2 active area (11.5 mm × 7 mm) of the PSC device was 19.06%, with J_{SC} = 22.25 mA/cm^2, V_{OC} = 1.145 V, and FF = 74.81% Figure S9a. Figure 2b shows the IPCE spectrum of our best-performing device along with the reflection (R) and transmission (T) spectra. The IPCE spectra of the devices based on different Pz:PFN ratios are shown in Figure S10. The dip in the external quantum efficiency (EQE) spectrum correlates well with the hump in the reflection spectra. The loss in the current density due to reflection can be calculated from the EQE and internal quantum efficiency (IQE) spectra using eqs S-E3 and S-E4 in the SI. The integrated $J_{SC,EQE}$ is calculated by

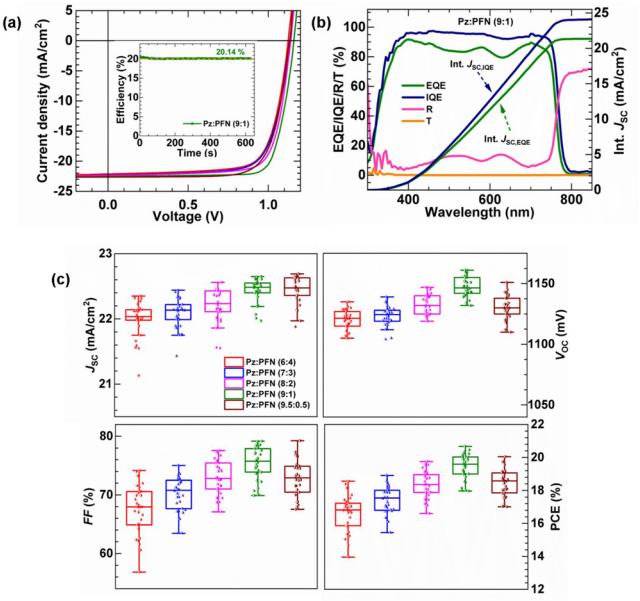

Figure 2. Color key − Pz:PFN (6:4) is red, Pz:PFN (7:3) is blue, Pz:PFN (8:2) is magenta, Pz:PFN (9:1) is olive color, and Pz:PFN (9.5:0.5) is wine color. (a) Current density vs voltage ($J-V$) characteristics of the photovoltaic devices under 1-Sun (100 mW/cm^2) condition in the forward scan direction. The forward and reverse $J-V$ scans of the representative devices are shown in Figure S9b. The inset figure represents the power output of the Pz:PFN (9:1) PSC device, taken under maximum power point tracking with stabilized efficiency, which is 20.14% (at 970 mV). (b) IPCE spectra of the best-performing Pz:PFN (9:1) PSC, including the reflection (R), transmission (T), and integrated current density (Int. J_{SC}). (c) Boxplots of short-circuit current density (J_{SC}), open-circuit voltage (V_{OC}), fill factor (FF), and power conversion efficiency (PCE%) over 30 devices.

integrating the EQE spectrum over the 1-Sun spectrum. There is a current density mismatch of less than 5% between the $J_{SC,EQE}$ and J_{SC} measured from the $J-V$ measurement, and this can be understood on the basis of the edge effect from the active area (17.5 mm^2, inset Figure S9c) of the device or pre-bias measurement condition.[37,38] To verify the reproducibility of the device performance with the Pz:PFN mixing engineering strategy, 30 devices of each mixing ratio were fabricated using the device procedure outlined in the experimental section in the SI. Figure 2c summarizes the distribution of photovoltaic parameters under a forward scan. The average performance improved from ∼17% for Pz:PFN (6:4) to >20% for Pz:PFN (9:1), with the narrowest distribution among 30 PSCs, i.e., highly reproducible, efficient PSCs. The performance improvement is attributed to the increases in J_{SC}, V_{OC}, and FF. The stabilized efficiency under maximum power point tracking for the Pz:PFN (9:1) PSC device is 20.14% (at 970 mV, inset Figure 2a), and for the Pz:PFN (6:4) PSC device is it 17.32% (at 920 mV, Figure S9c).

Numerous research reports have employed PFN-Br as an interlayer to overcome the hydrophobicity of polymeric HTLs such as PTAA to obtain a uniform perovskite film and even as an additive in the perovskite solution to improve its performance.[23,36,39] On the other hand, by looking at the structure of PFN-Br (Figure S12a), one can see the presence of a nonpolar long alkyl chain. This can cause severe wetting issues and therefore raises similar concerns about forming a

https://doi.org/10.1021/acsenergylett.3c01385
ACS Energy Lett. 2023, 8, 3860−3867

non-uniform perovskite layer. Moreover, the high water contact angle of PFN-Br, as shown in Figure S12b, corroborates the hypothesis. However, a uniform perovskite layer was formed after the incorporation of PFN-Br. This raises the point of how the perovskite layer is formed when highly hydrophobic PFN-Br is introduced. In the literature, the role of PFN-Br in helping to form a uniform perovskite layer has not been focused on yet. For instance, Wang et al. incorporated a PFN-Br interlayer in between the PTAA HTL and perovskite absorber layer and assumed the possibility of PFN-Br's redissolution during the deposition of the perovskite layer, thereby improving the device performance.[39] Therefore, it is of utmost importance to understand the underlying mechanism of a uniform perovskite layer formation on a PFN-Br interlayer or mixed Pz:PFN HTL. We noticed that PFN-Br is readily soluble in DMF and DMSO solvents (Figure S13) and allows us to make good-quality films, as shown in Figure S7 and by the domain analysis in Figure S14 with almost similar average domain sizes. Further, we deposited $MAPbI_3$ (without Br^-) independently on MeO-2PACz- and Pz:PFN-coated glass substrates. The $MAPbI_3$ perovskite film deposited on MeO-2PACz and Pz:PFN (9:1) is indistinctly uniform, as shown in Figure S15. XRD diffractograms were obtained for both films, as shown in Figure 3a. The XRD pattern of $MAPbI_3$ deposited on Pz:PFN HTL shows a peak with a lower full width at half-maximum (FWHM). A slight shift (~0.0024°) in the XRD peak is observed between the $MAPbI_3$ film deposited on the MeO-2PACz-coated glass substrate vs the $MAPbI_3$ film on the Pz:PFN (9:1)-coated glass substrate. The reason for this small shift is investigated via spectroscopic techniques, as the spectroscopic probes are known to be more sensitive than the structural probes. As per previous reports by us and others, microstructure synchrotron studies were found to be less conclusive than spectroscopic studies, where spectroscopy could provide essential insight to correlate with solar cells' performance.[40,41] These samples are tested for PL spectroscopy. The raw PL data show small peak-shift and FWHM differences. The FWHM of the MAPI film being broad on MeO-2PACz substrates could be explained based on the FWHM of the XRD peak. However, the peak-shift which was found to be red-shifted in raw data interestingly overlapped once an OD (or self-absorption) correction was introduced (Figures 3b and S16).[42] This suggests that bromine-containing Pz:PFN does not incorporate the Br^- ion into the absorber layer within the sensitivity limits of the structural and spectroscopic probes. A small peak shift on the higher degree side in the XRD peak falls near the resolution limit of the instrument, which is 0.0012°.

To further understand the interaction between PFN-Br and perovskite, a series of liquid-state ^1H NMR measurements in solution (deuterated DMSO) were performed, and the results are shown in Figure 3c–e (full-scale data shown in Fgure S17). Initially, a ^1H NMR spectrum of a triple-cation perovskite solution dissolved in deuterated DMSO was recorded (Figure 3c), showing a resonance peak at around 9 ppm, which corresponds to protons bound to the nitrogen atoms of formamidinium ($HC(NH_2)_2^+$ or FA^+) and methylammonium ($CH_3NH_3^+$ or MA^+). Upon addition of PFN-Br to the perovskite solution in deuterated DMSO, the peak at around 9 ppm splits into two new peaks due to the interaction between cationic $HC(NH_2)_2^+$ (FA^+)/$CH_3NH_3^+$ (MA^+) and PFN-Br. To further examine the interaction between MA^+ and PFN-Br,

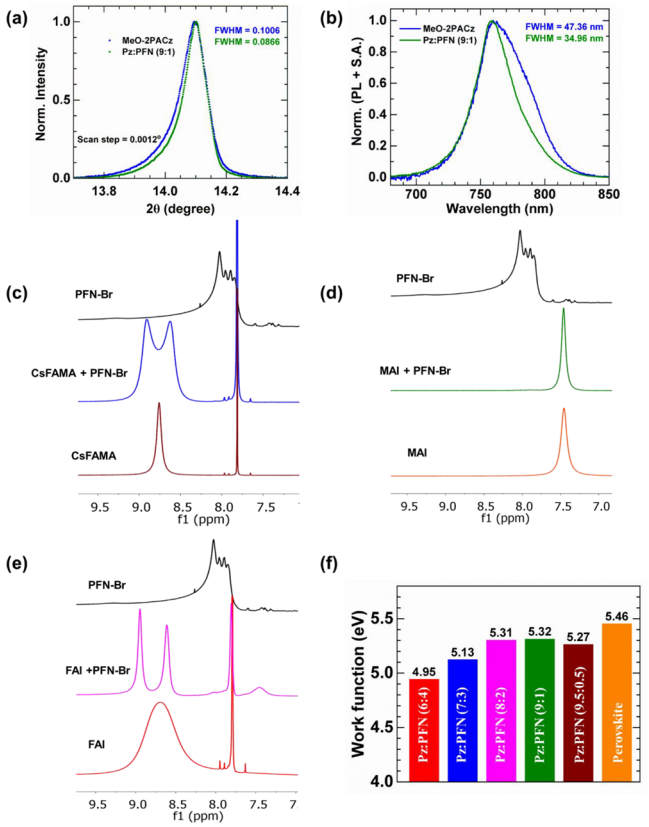

Figure 3. (a) XRD pattern and (b) PL spectra (self-absorption corrected) of the $MAPbI_3$ perovskite thin film (thickness ~250 nm) deposited on the MeO-2PACz- and Pz:PFN (9:1)-coated glass substrates.[42] (c) ^1H NMR of the CsFAMA, CsFAMA + PFN-Br, and PFN-Br solutions prepared in DMSO-d_6 solvent. (d) ^1H NMR of the MAI, MAI + PFN-Br, and PFN-Br solutions prepared in DMSO-d_6 solvent. (e) ^1H NMR of the FAI, FAI + PFN-Br, and PFN-Br solutions prepared in DMSO-d_6 solvent. (f) The work function of the Pz:PFN HTLs was measured using KPFM study.

an additional ^1H NMR experiment using only MAI without and with PFN-Br was carried out. As shown in Figure 3d, no peaks are split and shifted, indicating that the peak split in the perovskite solution with PFN-Br addition (Figure 3c) is related to the change in the FA^+ cation in the presence of PFN-Br. To further confirm this conclusion, we recorded a ^1H NMR spectrum of only FAI without and with PFN-Br. As shown in Figure 3e, this peak around 9 ppm of FAI solution with PFN-Br additive is split into two peaks in a way similar to the splitting observed in the perovskite solution with PFN-Br additive. The splitting of FA^+ protons into two new signals has also been observed by other research groups and is ascribed to the formation of hydrogen bond complexes of the amidinium moiety of the FA^+ cation.[43−46] Considering all NMR results, it is thus proposed that a hydrogen bond between FA^+ and PFN-Br exists, which might help in perovskite layer formation during its spin-coating step and crystallization and might also remain present in the final perovskite film and can be beneficial for prolonging device stability. In addition to the perovskite layer formation with an improved interfacial property, we hypothesized that the addition of PFN-Br might influence the electronic properties of Me-4PACz. Therefore, we measured the work function of Me-4PACz (without and with PFN-Br in different ratios) and perovskite using the KPFM technique.

https://doi.org/10.1021/acsenergylett.3c01385
ACS Energy Lett. 2023, 8, 3860−3867

The work function of the films is determined using gold as a reference, and the results are shown in Figures 3f, S18, and S19. Though the pristine Me-4PACz shows a better energy level alignment with the perovskite layer (Figure S19), forming the perovskite layer on pristine Me-4PACz is a challenge. Because of the effect of interface dipoles caused by the electrolyte moiety present in PFN-Br, the work function of Me-4PACz showed dramatic changes with the different mixing ratios. For the particular Pz:PFN (9:1) case, the energy level alignment matches closely with the Me-4PACz (without any PFN-Br) and also with the work function of the perovskite layer, implying better hole extraction efficacy. Moreover, we performed ultraviolet photoelectron spectroscopy (UPS) on the above-mentioned HTLs, and the Fermi levels were found to be well aligned with the KPFM results, as shown in Figure S19b. Further, the built-in potential difference (V_{bi}) calculated from the dark current characteristics of diodes shows a clear trend in reduced barrier voltage for the case of Pz:PFN (9:1) composition as compared with the other mixing ratio compositions, as seen in Figure S20. We observed a slight relative change in the EQE and corresponding J_{SC} (whether integrated or measured using an AM1.5G solar simulator light source), which can be seen modulating with respect to the V_{bi} values (Figure S20) of diodes. V_{bi} values modulate with respect to different Fermi levels of the ITO/(Pz:PFN::X:Y) layer, as ETL is common in all diodes (Figure S19).[47] This also explains the reason behind the high device efficiency in the Pz:PFN (9:1) case compared to the other cases despite a similar perovskite crystal structure and top surface morphology.

The dark current measurement can also give insights into the recombination at the perovskite and Pz:PFN interface by estimating the reverse saturation current density J_0.[48] Therefore, we measured the dark current of the devices with different ratios of Pz:PFN and observed the lowest dark current density J_D at −0.3 V of 5.28×10^{-6} mA/cm^2 and the reverse saturation current density J_0 of 2.20×10^{-10} mA/cm^2 for the Pz:PFN (9:1) (Figure S21a), whereas a typical J_0 value for established silicon photovoltaics is 10^{-10}−10^{-9} mA/cm^2.[49,50] The J_D and J_0 values of all of the devices with different Pz:PFN mixing ratios are tabulated in Table S6. The lowest J_D and J_0 values for the 9:1 case imply suppressed recombination at the perovskite/Pz:PFN interface. Figure 4a represents the variation in V_{OC} vs $\log_{10}(J_{sc}/J_0)$, where J_{SC} and J_0 are calculated from the illuminated and dark currents. The $\log_{10}(J_{SC}/J_0)$ is higher for Pz:PFN (9:1) (Figure S21b), and the corresponding V_{OC} is higher as per the basic diode equation.[51] Transient photovoltage (TPV) decay measurements were carried out to determine the charge carrier lifetime and to quantify the recombination process.[52,53] The normalized TPV decay profile, fitted with a monoexponential decay and measured for all the cases, is shown in Figure S22a. Among all the cases studied, the TPV decay profile of the device with Me-4PACz:PFN-Br (9:1) showed a slow decay and a high perturbed charge carrier lifetime (τ) (please refer to Table S7), implying suppressed nonradiative recombination.[54,55] This can be further correlated with the device V_{OC}. The V_{OC} of the device is calculated as a function of the perturbed charge carrier lifetime (τ) and high V_{OC} as in the 9:1 case (Figure 4b), implying the lower recombination. The dependence of V_{OC} on the incident light fluence was investigated for all of the Pz:PFN-based devices to get further insight into recombination processes. The incident light is varied from 100 mW/cm^2 (1 Sun) to 1 mW/cm^2 (0.01 Sun) with a set of neutral density (ND) filters. Figure S22b

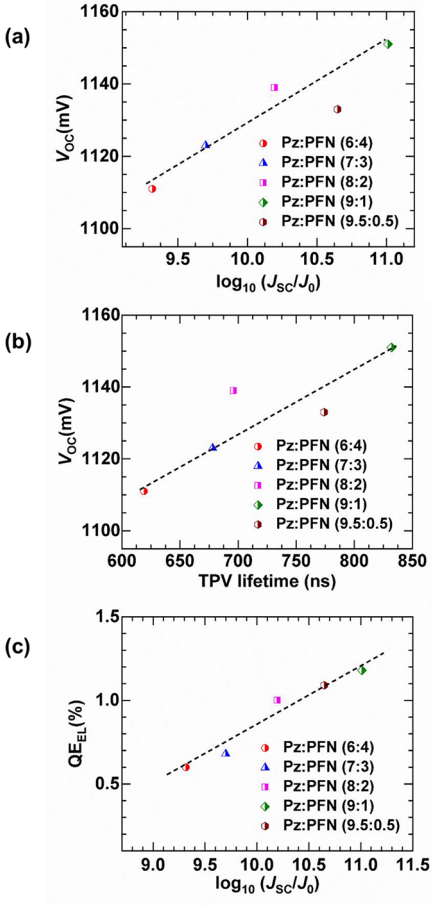

Figure 4. (a) V_{OC} of the representative devices as a function of short-circuit (J_{SC}) and reverse saturation current density (J_0). (b) V_{OC} of the representative devices as a function of the perturbed charge carrier lifetime measured from TPV measurement at 1-Sun illumination condition. (c) Electroluminescence (EL) quantum efficiency plotted as a function of J_{SC} and J_0.

(and Figure S23) plots V_{OC} against intensity in a natural logarithmic scale, and the slope corresponds to nkT_cq^{-1} where n, k, T_c, and q are the ideality factor, Boltzmann constant, room temperature of the device, and electronic charge, respectively.[56,57] The slope of the best-performing device, that is, employing Pz:PFN (9:1), gives an n value of 1.05 (Figure S22b) and is smallest when compared to those for other mixing ratios of Pz:PFN-based devices, implying suppressed nonradiative trap-assisted recombination. Ideality factor n being close to 1 suggests that the absorber is free from bulk defects and hence it provides higher V_{OC}.[48] Relatively, this higher V_{OC} (free from nonradiative recombination channel) further facilitates charge carrier extraction under short-circuit conditions, i.e., J_{SC} for optimal PSCs. The lower value of series resistance (~4 Ω/sq) calculated from the dark and illuminated current also indicates higher FF and V_{OC} for Pz:PFN (9:1), as shown in Figures S22c,d and S24.[58,59] The device performance is limited by the series resistance. If the devices are free from series resistance, then the FF will be higher and the reverse saturation current will be lower, which can be calculated from the Sun's V_{OC} measurement as shown in Figure S25.[60] The Sun's V_{OC}-based pseudo-J−V curve showed more than 2 orders of magnitude reduction in reverse saturation current density J_0 to a value of sub-picoampere (PA), i.e., 0.78 pA/cm^2, Figure S26 and Table S8.[61] We measured the electro-

https://doi.org/10.1021/acsenergylett.3c01385
ACS Energy Lett. 2023, 8, 3860−3867

luminescence quantum efficiency (QE_{EL}) of the PSCs and found it to be highest for the Pz:PFN(9:1), as shown in Figure S27 and Table S9. Figure 4c depicts the QE_{EL} plotted as a function of $\log_{10}(J_{sc}/J_0)$ and it can be seen that it is highest for the Pz:PFN (9:1). This again indicates that the Pz:PFN (9:1) HTL-based PSC interface has relatively fewer trap states, which is also verified from higher TPV lifetime (indicating the presence of fewer trap states).[62,63] A comparison of the PV parameters for the different mixing ratios of Me-4PACz and PFN-Br is tabulated in Table S10. Finally, we investigated the long-term stability of our best-performing Pz:PFN (9:1)-based device in comparison with Pz:PFN (6:4). The device performance was measured under relative humidity in a range of 40−50% and aged in a N_2-filled glovebox without sealing or encapsulation. Figure S28 shows the long-term stability of our best-performing device. After >3000 h of storage, the device retained T_{95} > 3000 h of the maximum device efficiency. Further, the morphological stability was investigated at 85 °C, and no significant degradation was observed (Figures S29 and S30). The operational stability at the 1-Sun condition and thermal stability at 85 °C of the unencapsulated device under N_2 environment retain >90% of the initial efficiency after 300 and 600 h, respectively (Figure S31). This improved device yield and stability can be ascribed not only to the uniform perovskite layer coverage on the Me-4PACz but also to the interfacial interaction of PFN-Br with the perovskite.

To summarize, we present a mixing engineering strategy of combining a Me-4PACz SAM with the conjugated polyelectrolyte PFN-Br polymer. The mixing of the PFN-Br with the Me-4PACz facilitates uniform deposition of the perovskite layer on top of the hydrophobic Me-4PACz HTL. The uniform deposition of the perovskite layer on the top of PFN-Br mixed Me-4PACz happened due to Me-4PACz: PFN-Br interaction with the A-site cation, which was confirmed via solution-state NMR. This further facilitates an improved crystallization of the perovskite layer, which was confirmed via narrow diffraction in XRD and narrow PL peaks results. In addition to this, the KPFM result reveals that mixing with PFN-Br tunes the work function of Me-4PACz and that, for the optimized 9:1 mixing ratio, the energy level alignment of Pz:PFN matches well with the perovskite. As a result of this, the perovskite device demonstrates high and reproducible efficiency of over 20%, concomitant with high stability for T_{95} > 3000 h when measured in relative humidity of ∼40%. We believe that the mixing engineering of the Me-4PACz SAM with the electrolyte polymer PFN-Br will not only open new doors to tackle hydrophobic SAMs in solution-processable efficient photovoltaic devices but also allow designing new electrolyte-based polymers and/or small molecules that can be combined with SAMs, thereby quilting a better interface.

■ ASSOCIATED CONTENT

Supporting Information

The Supporting Information is available free of charge at https://pubs.acs.org/doi/10.1021/acsenergylett.3c01385.

Experimental details, current density vs voltage ($J-V$) characteristics, SEM images, XRD pattern, EQE spectrum, absorption and photoluminescence spectra, full-scale NMR, KPFM and UPS results, dark current density vs voltage characteristics, TPV, ideality factor, intensity-dependent $J-V$, Suns V_{OC}, electroluminescence quantum efficiency (QE_{EL}), and device stability (PDF)

Video V1, showing perovskite deposition on the Me-4PACz-coated ITO substrate (MP4)

■ AUTHOR INFORMATION

Corresponding Authors

Ashish Kulkarni − *Helmholtz Young Investigator Group FRONTRUNNER, IEK5-Photovoltaik, Forschungszentrum Jülich, 52428 Jülich, Germany;* orcid.org/0000-0002-7945-208X; Email: a.kulkarni@fz-juelich.de, ashish.kulkarni786@gmail.com

Dinesh Kabra − *Department of Physics, Indian Institute of Technology Bombay, Mumbai 400076, India;* orcid.org/0000-0001-5256-1465; Email: dkabra@iitb.ac.in

Authors

Kashimul Hossain − *Department of Physics, Indian Institute of Technology Bombay, Mumbai 400076, India*

Urvashi Bothra − *Department of Physics, Indian Institute of Technology Bombay, Mumbai 400076, India*

Benjamin Klingebiel − *IEK-5 Photovoltaik, Forschungszentrum Jülich, 52428 Jülich, Germany*

Thomas Kirchartz − *IEK-5 Photovoltaik, Forschungszentrum Jülich, 52428 Jülich, Germany; Faculty of Engineering and CENIDE, University of Duisburg-Essen, 47057 Duisburg, Germany;* orcid.org/0000-0002-6954-8213

Michael Saliba − *Helmholtz Young Investigator Group FRONTRUNNER, IEK5-Photovoltaik, Forschungszentrum Jülich, 52428 Jülich, Germany; Institute for Photovoltaics (IPV), University of Stuttgart, 70569 Stuttgart, Germany;* orcid.org/0000-0002-6818-9781

Complete contact information is available at: https://pubs.acs.org/10.1021/acsenergylett.3c01385

Author Contributions

†K.H. and A.K. contributed equally to this work.

Notes

The authors declare no competing financial interest.

■ ACKNOWLEDGMENTS

This work was supported by the Ministry of New and Renewable Energy India: National Centre for Photovoltaic Research and Education (NCPRE) Phase III. This work was also partially supported by the Indo-Swedish joint project funded by DST-India (DST/INT/SWD/VR/P-20/2019). A.K. and M.S. thank the Helmholtz Young Investigator group FRONTRUNNER. M.S. thanks the German Research Foundation (DFG) for funding (SPP2196, 431314977/GRK 2642). M.S. acknowledges funding by ProperPhotoMile. Project ProperPhotoMile is supported under the umbrella of SOLARERA.NET co-funded by The Spanish Ministry of Science and Education and the AEI under Project PCI2020-112185 and CDTI Project IDI-20210171; the Federal Ministry for Economic Affairs and Energy based on a decision by the German Bundestag Projects FKZ 03EE1070B and FKZ 03EE1070A and the Israel Ministry of Energy with Project 220-11-031. SOLAR-ERA.NET is supported by the European Commission within the EU Framework Programme for Research and Innovation HORIZON 2020 (Cofund ERA-NET action number 786483) funded by the European Union. M.S. acknowledges funding from the European Research

Council under the Horizon Europe program (LOCAL-HEAT, Grant Agreement 101041809). M.S. acknowledges funding from the German Bundesministerium für Bildung and Forschung (BMBF), project "NETPEC" (01LS2103E).

REFERENCES

(1) Kojima, A.; Teshima, K.; Shirai, Y.; Miyasaka, T. Organometal Halide Perovskites as Visible-Light Sensitizers for Photovoltaic Cells. *J. Am. Chem. Soc.* **2009**, *131* (17), 6050−6051.
(2) Min, H.; Lee, D. Y.; Kim, J.; Kim, G.; Lee, K. S.; Kim, J.; Paik, M. J.; Kim, Y. K.; Kim, K. S.; Kim, M. G.; Shin, T. J.; Il Seok, S. Perovskite Solar Cells with Atomically Coherent Interlayers on SnO_2 Electrodes. *Nature* **2021**, *598* (7881), 444−450.
(3) Jeong, J.; Kim, M.; Seo, J.; Lu, H.; Ahlawat, P.; Mishra, A.; Yang, Y.; Hope, M. A.; Eickemeyer, F. T.; Kim, M.; et al. Pseudo-Halide Anion Engineering for α-$FAPbI_3$ Perovskite Solar Cells. *Nature* **2021**, *592* (7854), 381−385.
(4) Singh, S.; Laxmi; Kabra, D. Defects in Halide Perovskite Semiconductors: Impact on Photo-Physics and Solar Cell Performance. *J. Phys. D. Appl. Phys.* **2020**, *53* (50), 503003.
(5) Miyata, A.; Mitioglu, A.; Plochocka, P.; Portugall, O.; Wang, J. T. W.; Stranks, S. D.; Snaith, H. J.; Nicholas, R. J. Direct Measurement of the Exciton Binding Energy and Effective Masses for Charge Carriers in Organic-Inorganic Tri-Halide Perovskites. *Nat. Phys.* **2015**, *11* (7), 582−587.
(6) Hirasawa, M.; Ishihara, T.; Goto, T.; Uchida, K.; Miura, N. Magnetoabsorption of the Lowest Exciton in Perovskite-Type Compound $(CH_3NH_3)PbI_3$. *Phys. B Phys. Condens. Matter* **1994**, *201* (C), 427−430.
(7) Manser, J. S.; Christians, J. A.; Kamat, P. V. Intriguing Optoelectronic Properties of Metal Halide Perovskites. *Chem. Rev.* **2016**, *116* (21), 12956−13008.
(8) Kim, G.; Petrozza, A. Defect Tolerance and Intolerance in Metal-halide Perovskites. *Adv. Energy Mater.* **2020**, *10* (37), 2001959.
(9) Hossain, K.; Singh, S.; Kabra, D. Role of Monovalent Cations in the Dielectric Relaxation Processes in Hybrid Metal Halide Perovskite Solar Cells. *ACS Appl. Energy Mater.* **2022**, *5* (3), 3689−3697.
(10) Yao, Y.; Cheng, C.; Zhang, C.; Hu, H.; Wang, K.; De Wolf, S. Organic Hole-Transport Layers for Efficient, Stable, and Scalable Inverted Perovskite Solar Cells. *Adv. Mater.* **2022**, *34* (44), 2203794.
(11) Khadka, D. B.; Shirai, Y.; Yanagida, M.; Ryan, J. W.; Miyano, K. Exploring the Effects of Interfacial Carrier Transport Layers on Device Performance and Optoelectronic Properties of Planar Perovskite Solar Cells. *J. Mater. Chem. C* **2017**, *5* (34), 8819−8827.
(12) Degani, M.; An, Q.; Albaladejo-Siguan, M.; Hofstetter, Y. J.; Cho, C.; Paulus, F.; Grancini, G.; Vaynzof, Y. 23.7% Efficient Inverted Perovskite Solar Cells by Dual Interfacial Modification. *Sci. Adv.* **2021**, *7* (49), No. eabj7930.
(13) Tiwari, N.; Arianita Dewi, H.; Erdenebileg, E.; Narayan Chauhan, R.; Mathews, N.; Mhaisalkar, S.; Bruno, A. Advances and Potentials of NiO x Surface Treatments for p-i-n Perovskite Solar Cells. *Sol. RRL* **2022**, *6* (3), 2100700.
(14) Al-Ashouri, A.; Magomedov, A.; Roß, M.; Jošt, M.; Talaikis, M.; Chistiakova, G.; Bertram, T.; Márquez, J. A.; Köhnen, E.; Kasparavičius, E. Conformal Monolayer Contacts with Lossless Interfaces for Perovskite Single Junction and Monolithic Tandem Solar Cells. *Energy Environ. Sci.* **2019**, *12* (11), 3356−3369.
(15) Magomedov, A.; Al-Ashouri, A.; Kasparavičius, E.; Strazdaite, S.; Niaura, G.; Jošt, M.; Malinauskas, T.; Albrecht, S.; Getautis, V. Self-assembled Hole Transporting Monolayer for Highly Efficient Perovskite Solar Cells. *Adv. energy Mater.* **2018**, *8* (32), 1801892.
(16) Al-Ashouri, A.; Köhnen, E.; Li, B.; Magomedov, A.; Hempel, H.; Caprioglio, P.; Márquez, J. A.; Vilches, A. B. M.; Kasparavicius, E.; Smith, J. A.; et al. Monolithic Perovskite/Silicon Tandem Solar Cell with > 29% Efficiency by Enhanced Hole Extraction. *Science* **2020**, *370* (6522), 1300−1309.
(17) Levine, I.; Al-Ashouri, A.; Musiienko, A.; Hempel, H.; Magomedov, A.; Drevilkauskaite, A.; Getautis, V.; Menzel, D.; Hinrichs, K.; Unold, T.; Albrecht, S.; Dittrich, T. Charge Transfer Rates and Electron Trapping at Buried Interfaces of Perovskite Solar Cells. *Joule* **2021**, *5* (11), 2915−2933.
(18) Tockhorn, P.; Sutter, J.; Cruz, A.; Wagner, P.; Jäger, K.; Yoo, D.; Lang, F.; Grischek, M.; Li, B.; Li, J.; et al. Nano-Optical Designs for High-Efficiency Monolithic Perovskite−Silicon Tandem Solar Cells. *Nat. Nanotechnol.* **2022**, *17* (11), 1214−1221.
(19) Farag, A.; Feeney, T.; Hossain, I. M.; Schackmar, F.; Fassl, P.; Kuster, K.; Bauerle, R.; Ruiz-Preciado, M. A.; Hentschel, M.; Ritzer, D. B.; et al. Evaporated Self-Assembled Monolayer Hole Transport Layers: Lossless Interfaces in p-i-n Perovskite Solar Cells. *Adv. Energy Mater.* **2023**, *13*, 1614−6832.
(20) Datta, K.; Wang, J.; Zhang, D.; Zardetto, V.; Remmerswaal, W. H. M.; Weijtens, C. H. L.; Wienk, M. M.; Janssen, R. A. J. Monolithic All-Perovskite Tandem Solar Cells with Minimized Optical and Energetic Losses. *Adv. Mater.* **2022**, *34* (11), 2110053.
(21) Al-Ashouri, A.; Marčinskas, M.; Kasparavičius, E.; Malinauskas, T.; Palmstrom, A.; Getautis, V.; Albrecht, S.; McGehee, M. D.; Magomedov, A. Wettability Improvement of a Carbazole-Based Hole-Selective Monolayer for Reproducible Perovskite Solar Cells. *ACS Energy Lett.* **2023**, *8* (2), 898−900.
(22) Taddei, M.; Smith, J. A.; Gallant, B. M.; Zhou, S.; Westbrook, R. J. E.; Shi, Y.; Wang, J.; Drysdale, J. N.; McCarthy, D. P.; Barlow, S.; et al. Ethylenediamine Addition Improves Performance and Suppresses Phase Instabilities in Mixed-Halide Perovskites. *ACS Energy Lett.* **2022**, *7* (12), 4265−4273.
(23) Taylor, A. D.; Sun, Q.; Goetz, K. P.; An, Q.; Schramm, T.; Hofstetter, Y.; Litterst, M.; Paulus, F.; Vaynzof, Y. A General Approach to High-Efficiency Perovskite Solar Cells by Any Antisolvent. *Nat. Commun.* **2021**, *12* (1), 1−11.
(24) Diekmann, J.; Caprioglio, P.; Futscher, M. H.; Le Corre, V. M.; Reichert, S.; Jaiser, F.; Arvind, M.; Toro, L. P.; Gutierrez-Partida, E.; Peña-Camargo, F.; et al. Pathways toward 30% Efficient Single-Junction Perovskite Solar Cells and the Role of Mobile Ions. *Sol. RRL* **2021**, *5* (8), 2100219.
(25) Hu, L.; Zhang, L.; Ren, W.; Zhang, C.; Wu, Y.; Liu, Y.; Sun, Q.; Dai, Z.; Cui, Y.; Cai, L.; Zhu, F.; Hao, Y. High e Fficiency Perovskite Solar Cells with PTAA Hole Transport Layer Enabled by PMMA: F4-TCNQ Buried Interface Layer. *J. Mater. Chem. C* **2022**, *10* (26), 9714−9722.
(26) Dai, J.; Xiong, J.; Liu, N.; He, Z.; Zhang, Y.; Zhan, S.; Fan, B.; Liu, W.; Huang, X.; Hu, X.; et al. Synergistic Dual-Interface Modification Strategy for Highly Reproducible and Efficient PTAA-Based Inverted Perovskite Solar Cells. *Chem. Eng. J.* **2023**, *453*, 139988.
(27) Kuan, C.-H.; Luo, G.-S.; Narra, S.; Maity, S.; Hiramatsu, H.; Tsai, Y.-W.; Lin, J.-M.; Hou, C.-H.; Shyue, J.-J.; Diau, E. W.-G. How Can a Hydrophobic Polymer PTAA Serve as a Hole-Transport Layer for an Inverted Tin Perovskite Solar Cell? *Chem. Eng. J.* **2022**, *450*, 138037.
(28) Deng, X.; Qi, F.; Li, F.; Wu, S.; Lin, F. R.; Zhang, Z.; Guan, Z.; Yang, Z.; Lee, C.; Jen, A. K. Co-assembled Monolayers as Hole-Selective Contact for High-Performance Inverted Perovskite Solar Cells with Optimized Recombination Loss and Long-Term Stability. *Angew. Chem., Int. Ed.* **2022**, *61* (30), No. e202203088.
(29) Li, L.; Wang, Y.; Wang, X.; Lin, R.; Luo, X.; Liu, Z.; Zhou, K.; Xiong, S.; Bao, Q.; Chen, G.; et al. Flexible All-Perovskite Tandem Solar Cells Approaching 25% Efficiency with Molecule-Bridged Hole-Selective Contact. *Nat. Energy* **2022**, *7*, 708.
(30) Ehrler, B.; Ho-Baillie, A. W. Y.; Hutter, E. M.; Milić, J. V.; Tayebjee, M. J. Y.; Wilson, M. W. B. Scalable Ways to Break the Efficiency Limit of Single-Junction Solar Cells. *Appl. Phys. Lett.* **2022**, *120*, 10402.
(31) Yadav, H. O. S.; Kuo, A.-T.; Urata, S.; Shinoda, W. Effect of the Packing Density on the Surface Hydrophobicity of ω-Functionalized ($-CF_3$, $-CH_3$, $-OCH_3$, and $-OH$) Self-Assembled Monolayers: A Molecular Dynamics Study. *J. Phys. Chem. C* **2020**, *124* (26), 14237−14244.

(32) Godawat, R.; Jamadagni, S. N.; Garde, S. Characterizing Hydrophobicity of Interfaces by Using Cavity Formation, Solute Binding, and Water Correlations. *Proc. Natl. Acad. Sci. U. S. A.* **2009**, *106* (36), 15119−15124.
(33) Gao, Y.; Duan, L.; Guan, S.; Gao, G.; Cheng, Y.; Ren, X.; Wang, Y. The Effect of Hydrophobic Alkyl Chain Length on the Mechanical Properties of Latex Particle Hydrogels. *RSC Adv.* **2017**, *7* (71), 44673−44679.
(34) Chen, W.; Karde, V.; Cheng, T. N. H.; Ramli, S. S.; Heng, J. Y. Y. Surface Hydrophobicity: Effect of Alkyl Chain Length and Network Homogeneity. *Front. Chem. Sci. Eng.* **2021**, *15* (1), 90−98.
(35) Bakulin, A. A.; Pshenichnikov, M. S.; Bakker, H. J.; Petersen, C. Hydrophobic Molecules Slow down the Hydrogen-Bond Dynamics of Water. *J. Phys. Chem. A* **2011**, *115* (10), 1821−1829.
(36) Moot, T.; Patel, J. B.; McAndrews, G.; Wolf, E. J.; Morales, D.; Gould, I. E.; Rosales, B. A.; Boyd, C. C.; Wheeler, L. M.; Parilla, P. A.; et al. Temperature Coefficients of Perovskite Photovoltaics for Energy Yield Calculations. *ACS Energy Lett.* **2021**, *6* (5), 2038−2047.
(37) Saliba, M.; Etgar, L. Current Density Mismatch in Perovskite Solar Cells. *ACS Energy Lett.* **2020**, *5* (9), 2886−2888.
(38) Singh, S.; Shourie, R. J.; Kabra, D. Efficient and Thermally Stable $CH_3NH_3PbI_3$ Based Perovskite Solar Cells with Double Electron and Hole Extraction Layers. *J. Phys. D. Appl. Phys.* **2019**, *52* (25), 255106.
(39) Wang, H.; Song, Y.; Kang, Y.; Dang, S.; Feng, J.; Dong, Q. Reducing Photovoltage Loss at the Anode Contact of Methylammonium-Free Inverted Perovskite Solar Cells by Conjugated Polyelectrolyte Doping. *J. Mater. Chem. A* **2020**, *8* (15), 7309−7316.
(40) Jain, N.; Chandrasekaran, N.; Sadhanala, A.; Friend, R. H.; McNeill, C. R.; Kabra, D. Interfacial Disorder in Efficient Polymer Solar Cells: The Impact of Donor Molecular Structure and Solvent Additives. *J. Mater. Chem. A* **2017**, *5* (47), 24749−24757.
(41) Huang, W.; Gann, E.; Thomsen, L.; Dong, C.; Cheng, Y. B.; McNeill, C. R. Unraveling the Morphology of High Efficiency Polymer Solar Cells Based on the Donor Polymer PBDTTT-EFT. *Adv. Energy Mater.* **2015**, *5* (7), 1401259.
(42) Saba, M.; Cadelano, M.; Marongiu, D.; Chen, F.; Sarritzu, V.; Sestu, N.; Figus, C.; Aresti, M.; Piras, R.; Geddo Lehmann, A.; et al. Correlated Electron-Hole Plasma in Organometal Perovskites. *Nat. Commun.* **2014**, *5* (1), 5049.
(43) Gong, J.; Yang, M.; Ma, X.; Schaller, R. D.; Liu, G.; Kong, L.; Yang, Y.; Beard, M. C.; Lesslie, M.; Dai, Y.; et al. Electron−Rotor Interaction in Organic−Inorganic Lead Iodide Perovskites Discovered by Isotope Effects. *J. Phys. Chem. Lett.* **2016**, *7* (15), 2879−2887.
(44) Sutter-Fella, C. M.; Li, Y.; Amani, M.; Ager, J. W.; Toma, F. M.; Yablonovitch, E.; Sharp, I. D.; Javey, A. High Photoluminescence Quantum Yield in Band Gap Tunable Bromide Containing Mixed Halide Perovskites. *Nano Lett.* **2016**, *16* (1), 800−806.
(45) Van Gompel, W. T. M.; Herckens, R.; Reekmans, G.; Ruttens, B.; D'Haen, J.; Adriaensens, P.; Lutsen, L.; Vanderzande, D. Degradation of the Formamidinium Cation and the Quantification of the Formamidinium-Methylammonium Ratio in Lead Iodide Hybrid Perovskites by Nuclear Magnetic Resonance Spectroscopy. *J. Phys. Chem. C* **2018**, *122* (8), 4117−4124.
(46) Alanazi, A. Q.; Kubicki, D. J.; Prochowicz, D.; Alharbi, E. A.; Bouduban, M. E. F.; Jahanbakhshi, F.; Mladenović, M.; Milić, J. V.; Giordano, F.; Ren, D.; et al. Atomic-Level Microstructure of Efficient Formamidinium-Based Perovskite Solar Cells Stabilized by 5-Ammonium Valeric Acid Iodide Revealed by Multinuclear and Two-Dimensional Solid-State NMR. *J. Am. Chem. Soc.* **2019**, *141* (44), 17659−17669.
(47) Siebert-Henze, E.; Lyssenko, V. G.; Fischer, J.; Tietze, M.; Brueckner, R.; Schwarze, M.; Vandewal, K.; Ray, D.; Riede, M.; Leo, K. Built-in Voltage of Organic Bulk Heterojuction p-i-n Solar Cells Measured by Electroabsorption Spectroscopy. *AIP Adv.* **2014**, *4* (4), 47134.
(48) Barnes, P. R. F.; Anderson, A. Y.; Juozapavicius, M.; Liu, L.; Li, X.; Palomares, E.; Forneli, A.; O'Regan, B. C. Factors Controlling Charge Recombination under Dark and Light Conditions in Dye Sensitised Solar Cells. *Phys. Chem. Chem. Phys.* **2011**, *13* (8), 3547−3558.
(49) Battaglia, C.; Cuevas, A.; De Wolf, S. High-Efficiency Crystalline Silicon Solar Cells: Status and Perspectives. *Energy Environ. Sci.* **2016**, *9* (5), 1552−1576.
(50) Woehl, R.; Gundel, P.; Krause, J.; Rühle, K.; Heinz, F. D.; Rauer, M.; Schmiga, C.; Schubert, M. C.; Warta, W.; Biro, D. Evaluating the Aluminum-Alloyed p^+-Layer of Silicon Solar Cells by Emitter Saturation Current Density and Optical Microspectroscopy Measurements. *IEEE Trans. Electron Devices* **2011**, *58* (2), 441−447.
(51) Sze, S. M.; Li, Y.; Ng, K. K. *Physics of Semiconductor Devices*; John Wiley & Sons, 2021.
(52) Kiermasch, D.; Baumann, A.; Fischer, M.; Dyakonov, V.; Tvingstedt, K. Revisiting Lifetimes from Transient Electrical Characterization of Thin Film Solar Cells; a Capacitive Concern Evaluated for Silicon, Organic and Perovskite Devices. *Energy Environ. Sci.* **2018**, *11* (3), 629−640.
(53) Krückemeier, L.; Liu, Z.; Krogmeier, B.; Rau, U.; Kirchartz, T. Consistent Interpretation of Electrical and Optical Transients in Halide Perovskite Layers and Solar Cells. *Adv. Energy Mater.* **2021**, *11* (46), 2102290.
(54) Kim, M.; Jeong, J.; Lu, H.; Lee, T. K.; Eickemeyer, F. T.; Liu, Y.; Choi, I. W.; Choi, S. J.; Jo, Y.; Kim, H.-B. Conformal Quantum Dot−SnO_2 Layers as Electron Transporters for Efficient Perovskite Solar Cells. *Science* **2022**, *375* (6578), 302−306.
(55) Singh, S.; Banappanavar, G.; Kabra, D. Correlation between Charge Transport Length Scales and Dielectric Relaxation Time Constant in Hybrid Halide Perovskite Semiconductors. *ACS Energy Lett.* **2020**, *5* (3), 728−735.
(56) Wetzelaer, G. J. A. H.; Kuik, M.; Blom, P. W. M. IdenTifying the Nature of Charge Recombination in Organic Solar Cells from Charge-Transfer State Electroluminescence. *Adv. Energy Mater.* **2012**, *2* (10), 1232−1237.
(57) Du, X.; Li, X.; Chen, Q.; Lin, H.; Tao, S. High Performance Organic Solar Cells Based on ZnO: POT2T as an Effective Cathode Interfacial Layer. *J. Phys.: Conf. Ser.* **2020**, *1549*, 42015 DOI: 10.1088/1742-6596/1549/4/042015.
(58) Liu, Z.; Siekmann, J.; Klingebiel, B.; Rau, U.; Kirchartz, T. Interface Optimization via Fullerene Blends Enables Open-Circuit Voltages of 1.35 V in $CH_3NH_3Pb(I_{0.8}Br_{0.2})_3$ Solar Cells. *Adv. Energy Mater.* **2021**, *11* (16), 2003386.
(59) Aberle, A. G.; Wenham, S. R.; Green, M. A. New Method for Accurate Measurements of the Lumped Series Resistance of Solar Cells. *Conference Record of the IEEE Photovoltaic Specialists Conference*; IEEE, 1993; pp 133−139. DOI: 10.1109/pvsc.1993.347065.
(60) Sinton, R. A.; Cuevas, A. A Quasi-Steady-State Open-Circuit Voltage Method for Solar Cell Characterization. In *16th European Photovoltaic Solar Energy Conference*; Scheer, H., McNelis, B., Palz, W., Ossenbrink, H. A., Helm, P., Eds.; Taylor and Francis, 2000; Vol. *1152*, pp 1−4. citeulike-article-id: 6901946.
(61) Yoshikawa, K.; Kawasaki, H.; Yoshida, W.; Irie, T.; Konishi, K.; Nakano, K.; Uto, T.; Adachi, D.; Kanematsu, M.; Uzu, H.; Yamamoto, K. Silicon Heterojunction Solar Cell with Interdigitated Back Contacts for a Photoconversion Efficiency over 26. *Nat. Energy* **2017**, *2* (5), 1−8.
(62) Lu, L. P.; Kabra, D.; Friend, R. H. Barium Hydroxide as an Interlayer between Zinc Oxide and a Luminescent Conjugated Polymer for Light-Emitting Diodes. *Adv. Funct. Mater.* **2012**, *22* (19), 4165−4171.
(63) Haddad, J.; Krogmeier, B.; Klingebiel, B.; Krückemeier, L.; Melhem, S.; Liu, Z.; Hüpkes, J.; Mathur, S.; Kirchartz, T. Analyzing Interface Recombination in Lead-Halide Perovskite Solar Cells with Organic and Inorganic Hole-Transport Layers. *Adv. Mater. Interfaces* **2020**, *7* (16), 2000366.